Supporting Information (SI) for:

Aqueous Zn-ion batteries using amorphous Zn-buserite with high activity and stability

Zhi-Qiang Wang[a,b], Xiao-Dong Liu[a,b], Hong-Ming Chen[a,b], Xiang-Yu Zhu[c], Li-Ying Song[a,b], Yun-Guo Yang[a,b] Jing Bai[a,b], M.J. Kim[c], Woon-Ming Lau[a,b,], Federico Rosei[d,]* and Dan Zhou[a,b,]**

[a] Beijing Advanced Innovation Center for Materials Genome Engineering, School of Mathematics and Physics, University of Science and Technology Beijing, Beijing 100083, China

[b] Shunde Innovation School, University of Science and Technology Beijing, Foshan, Guangdong 528000, China

[c] Department of Materials Science and Engineering, University of Texas Dallas, Richardson, TX, 75080, USA

[d] INRS Centre for Energy, Materials and Telecommunications, 1650 Boul. Lionel Boulet, Varennes (Quebec), J3X 1P7, Canada

*Corresponding authors:

leolau@ustb.edu.cn (W. M. Lau); rosei@emt.inrs.ca (F. Rosei); zhoudan@ustb.edu.cn (D. Zhou)

Physicochemical features comparison of PrGO and rGO

The physicochemical characteristics of rGO and PrGO were first investigated by transmission electron microscope (TEM), Raman spectroscopy, XPS, water contact angle and nitrogen adsorption/desorption measurements. The TEM images of rGO (**Fig. S1a**) and PrGO (**Fig. S1b**) confirm the successful formation of pores on the PrGO sheets, and the pore diameter ranges from several nano- to micro-meters.

Both Raman spectra shown in **Fig. S2** display characteristic peaks of graphene,[S1-S3] including one D band at 1351 cm^{-1} and one G band at 1591 cm^{-1}. Generally, the G band represents the E_{2g} phonon of sp^2-hybridized carbon atoms, which is attributed to ordered graphitic carbon. The D band is mainly ascribed to the sp^3-hybridized carbon, and disarranged/disordered carbon structures, such as amorphous carbon, grain boundaries and vacancies, contribute to this band. The intensity ratio of G and D band (I_G/I_D) of PrGO is 0.88, lower than that of rGO (1.0), due to the C=C bond of the graphene hexatomic ring being broken during pore-making process.[S4] The lower I_G/I_D of PrGO also indicate the increase of defects on PrGO sheets.[S4]

The XPS spectra of PrGO and rGO are shown in **Fig. S3.** The C 1s peak of both samples can be fitted to three peaks centered at 284.8, 286.5 and 288.1 eV, attributed to the C-C/C=C, C-O, and C=O bonds, respectively. The O 1s peak can be split into two peaks at 531.2 (C=O) and 533.2 eV (C-O). After comparison of the C 1s and O 1s peaks, we can conclude that the pore-making process increases the percentage of O, from 6.2% for rGO to 18.9% for PrGO. The higher O content and defects can improve the hydrophilic performance of PrGO, as confirmed by the water contact angle tests shown in **Fig. S4a** (the contact angle of PrGO is 12°, much lower than that of rGO, 60°). The hydrophilic PrGO can help the nucleation and growth of MnO_x on its surface, which is beneficial to uniformly coat MnO_x on PrGO sheets. The survey XPS spectra of PrGO and rGO are shown in **Fig. S5a.** Only peaks of C and O are observed, indicating that the chemical residues, including Ag, K, Mn element and their compounds, are fully removed after heat refluxing as well as washing by DIW.

Moreover, pores fabrication also increases the BET (Brunauer-Emmet-Teller) surface area (S_{BET} shown in Table S1). The S_{BET} of PrGO is 630 $m^2\ g^{-1}$, which is far higher than that of rGO (433 $m^2\ g^{-1}$). The larger S_{BET} means that PrGO can provide more active sites for the nucleation of MnO and for the storage of Zn ions.

The fabrication of pores on PrGO is important to improve the wettability of PrGO-MnO_x by eliminating the shielding effects of rGO. Therefore, the wettability of PrGO-MnO_x is much better than that of rGO-MnO_x, as suggested by the electrolyte (2 M $C_2F_6O_6S_2Zn$ + 0.2 M $C_2F_6O_6S_2Mn$) contact angles of rGO-MnO_x and PrGO-MnO_x electrode in **Fig. S4b**.

Table S1. Comparison of the BET surface area of rGO, PrGO and PrGO-MnO_x.

Samples	**S_{BET} (m^2 g^{-1})** [a]
rGO	433
PrGO	630
PrGO-MnO_x	210.4

Note [a]: the S_{BET} (specific surface area) derived by multipoint BET model.[S5]

Table S2. The electrochemical rate performance data of PrGO-MnO_x electrode.

Current Density (A g^{-1})	PrGO-MnO_x //Zn half- cell (mAh g^{-1})	PrGO-MnO_x //AQ full- cell (mAh g^{-1})
0.1	326	305
0.2	312	-
0.3	269	232
0.5	229	176
0.8	-	137
1.0	198	108
1.2	-	85
1.4	-	64
1.5	185	-
1.6	-	48
1.8	172	-
2.0	160	-
2.5	151	-

Fick's second law

Fick's second law can be described by the following equation.

$$D_{K^+} = \frac{4}{\pi\tau}\left(\frac{m_B V_M}{M_B S}\right)^2\left(\frac{\Delta E_S}{\Delta E_t}\right)^2 \quad \textbf{(Eq. S1)}$$

Where,

τ is the constant current pulse time,

m_B is the weight of the active material,

V_M is the molar volume of the active material,

M_B is the molar mass of the active material,

S is the active surface area of electrolyte-electrode interface,

ΔEs is the voltage change between the steady and original states at the plateau potential,

ΔEt is the total voltage-change during the current pulse time τ excluding the iR drop.

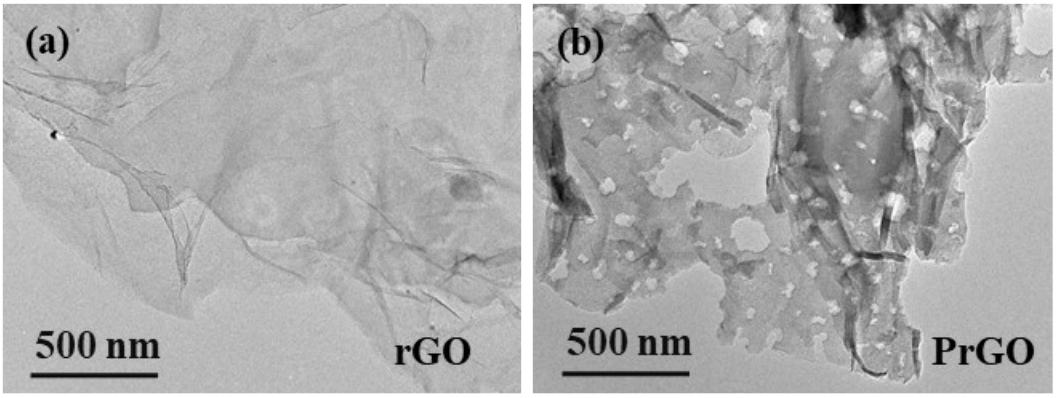

Fig. S1. TEM images of (**a**) rGO and (**b**) PrGO.

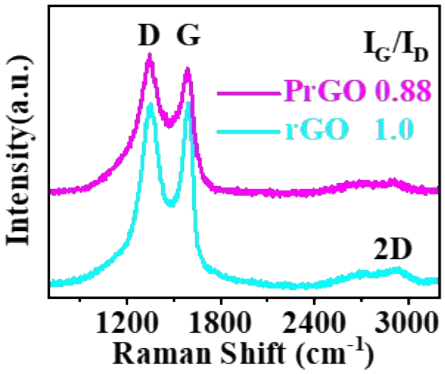

Fig. S2. Raman spectra of rGO and PrGO.

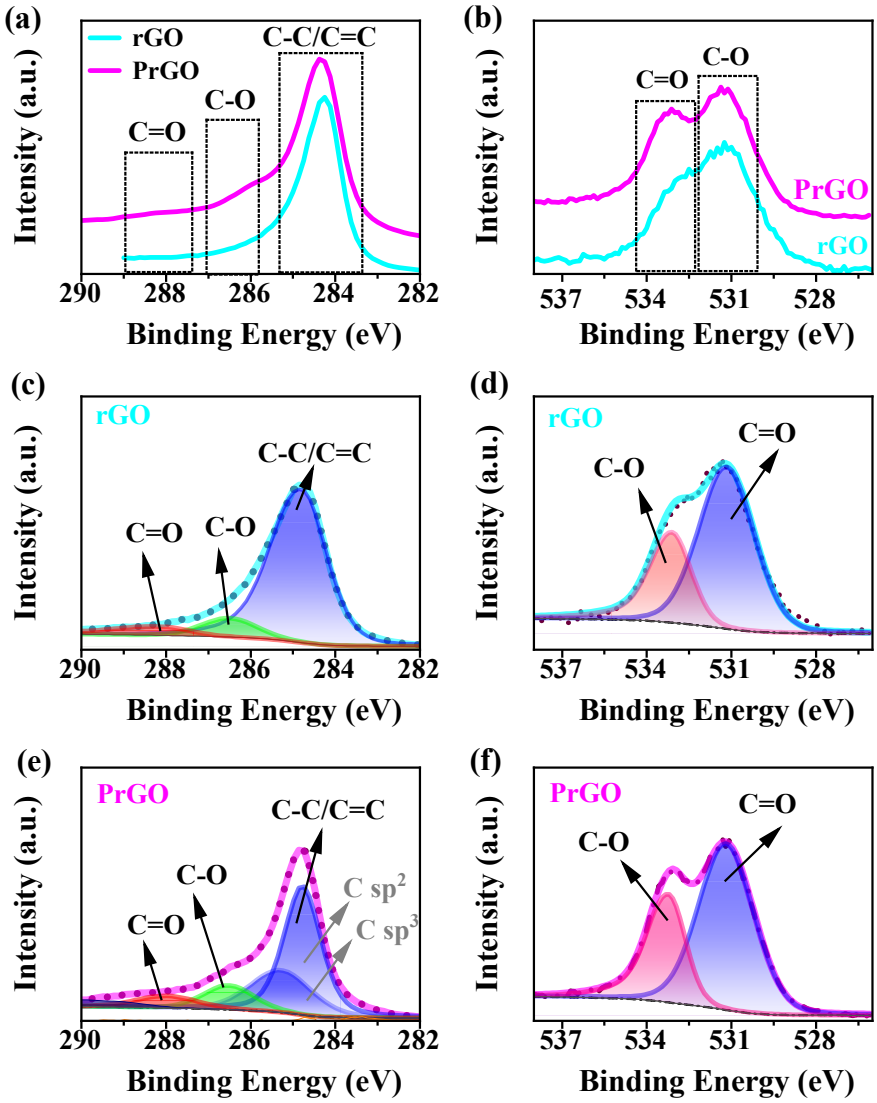

Fig. S3. (**a**) C 1s XPS spectra of rGO and PrGO. (**b**) O 1s XPS spectra of rGO and PrGO. The peak-fitted high-resolution XPS spectrum of C 1s and O 1s for **(c, d)** rGO and **(e, f)** PrGO.

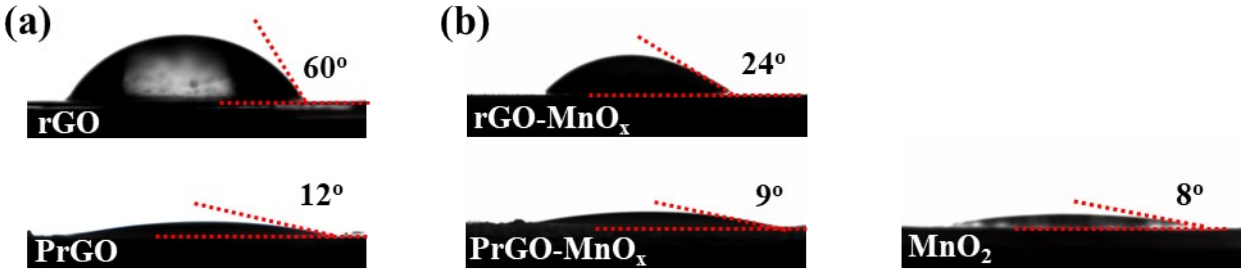

Fig. S4. (**a**) Water contact angles of rGO and PrGO. (**b**) Electrolyte (2 M $C_2F_6O_6S_2Zn$ + 0.2 M $C_2F_6O_6S_2Mn$) contact angles of rGO-MnO_x, PrGO-MnO_x and MnO_2 electrodes. The electrolyte contact angles are captured at the moment of just contact between electrolyte and electrodes.

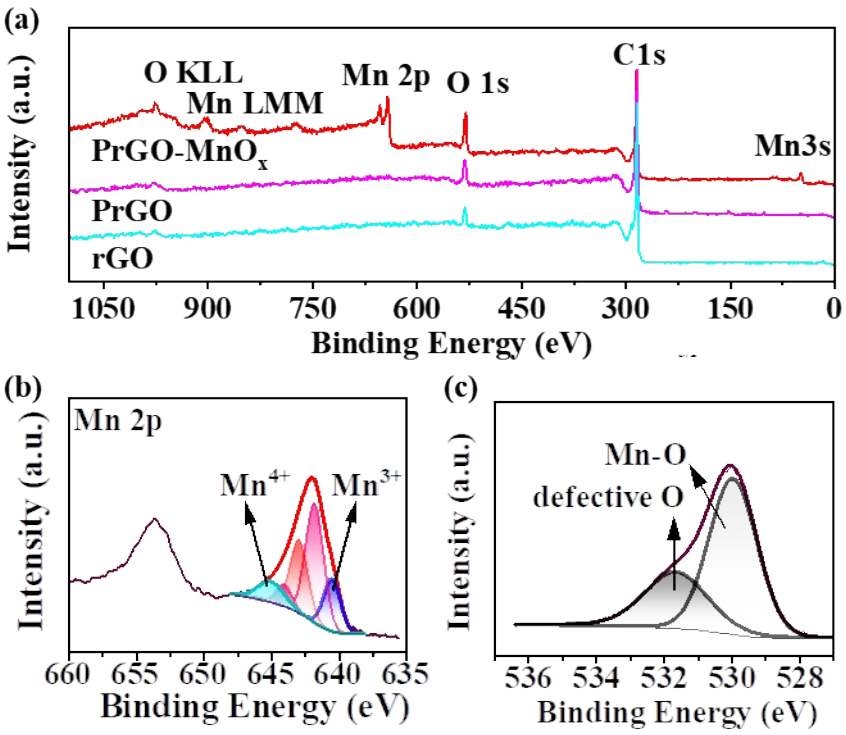

Fig. S5. (a) XPS survey spectrum of rGO, PrGO and PrGO-MnO_x. **(b)** Mn 2p spectrum of PrGO-MnO_x. **(c)** O 1s spectrum of A-MnO_x.

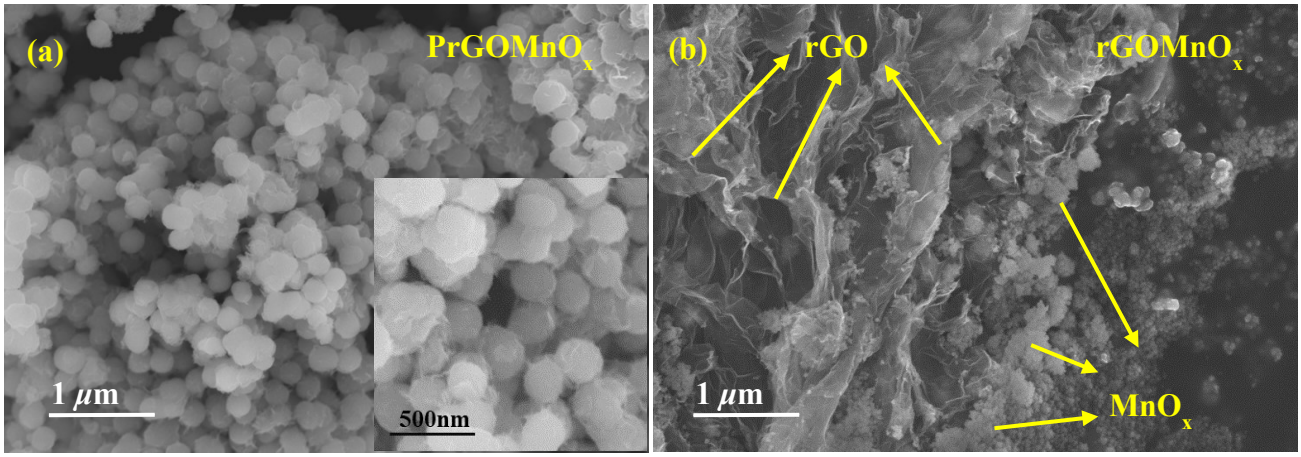

Fig. S6. SEM images of (**a**) PrGO-MnO_x and (**b**) rGO-MnO_x.

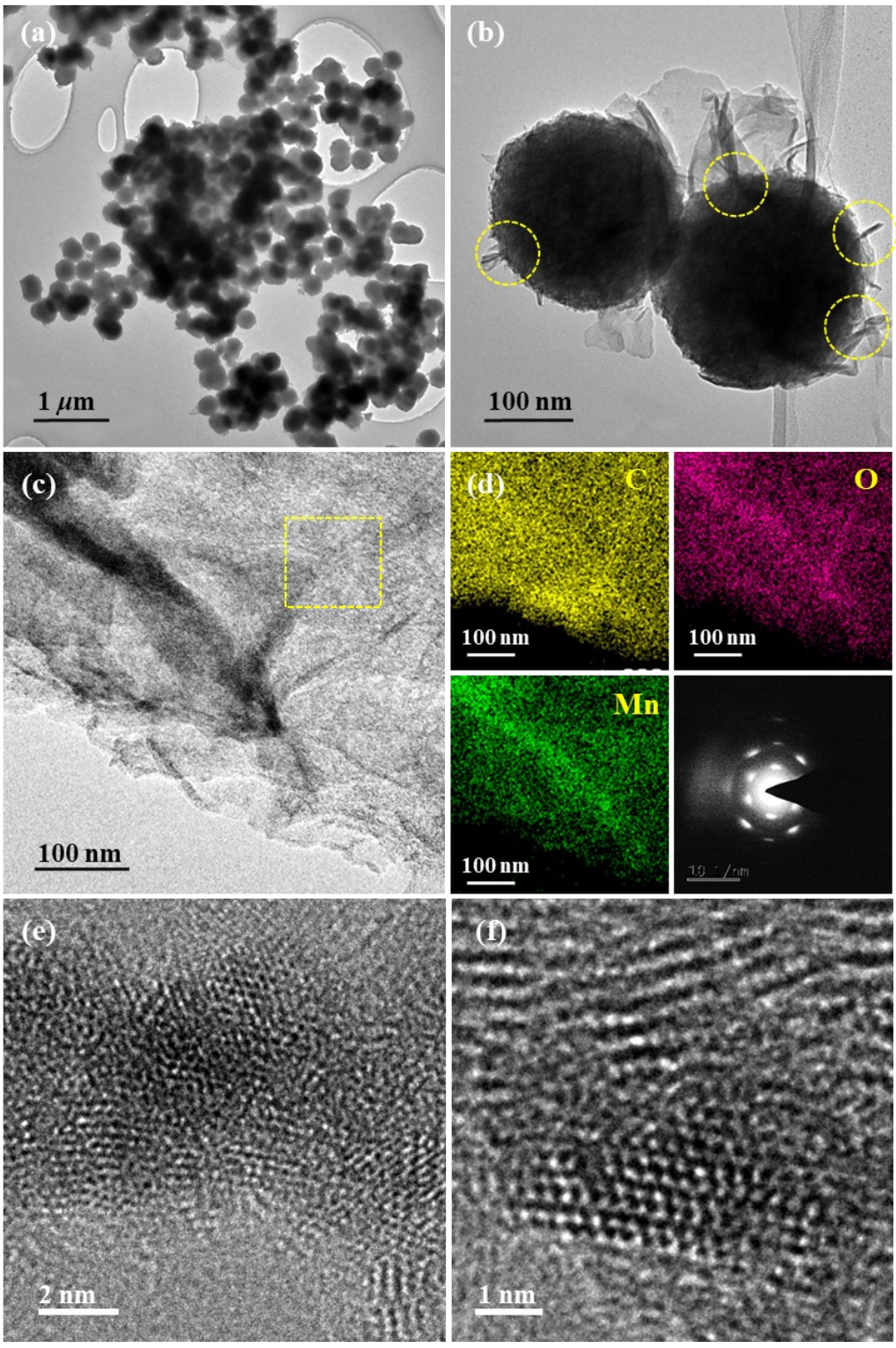

Fig. S7. (**a**) TEM images of PrGO-MnO_x. (**b**) Mapping images of PrGO-MnO_x. (**c** and **d**) TEM images of a PrGO sheet (from PrGO-MnO_x sample) coated by MnO_x, and corresponding mapping images (acquired from yellow marked area). (**e** and **f**) HRTEM images of MnO_x phase in PrGO-MnO_x, which exhibit the short-range order structure in PrGO-MnO_x.

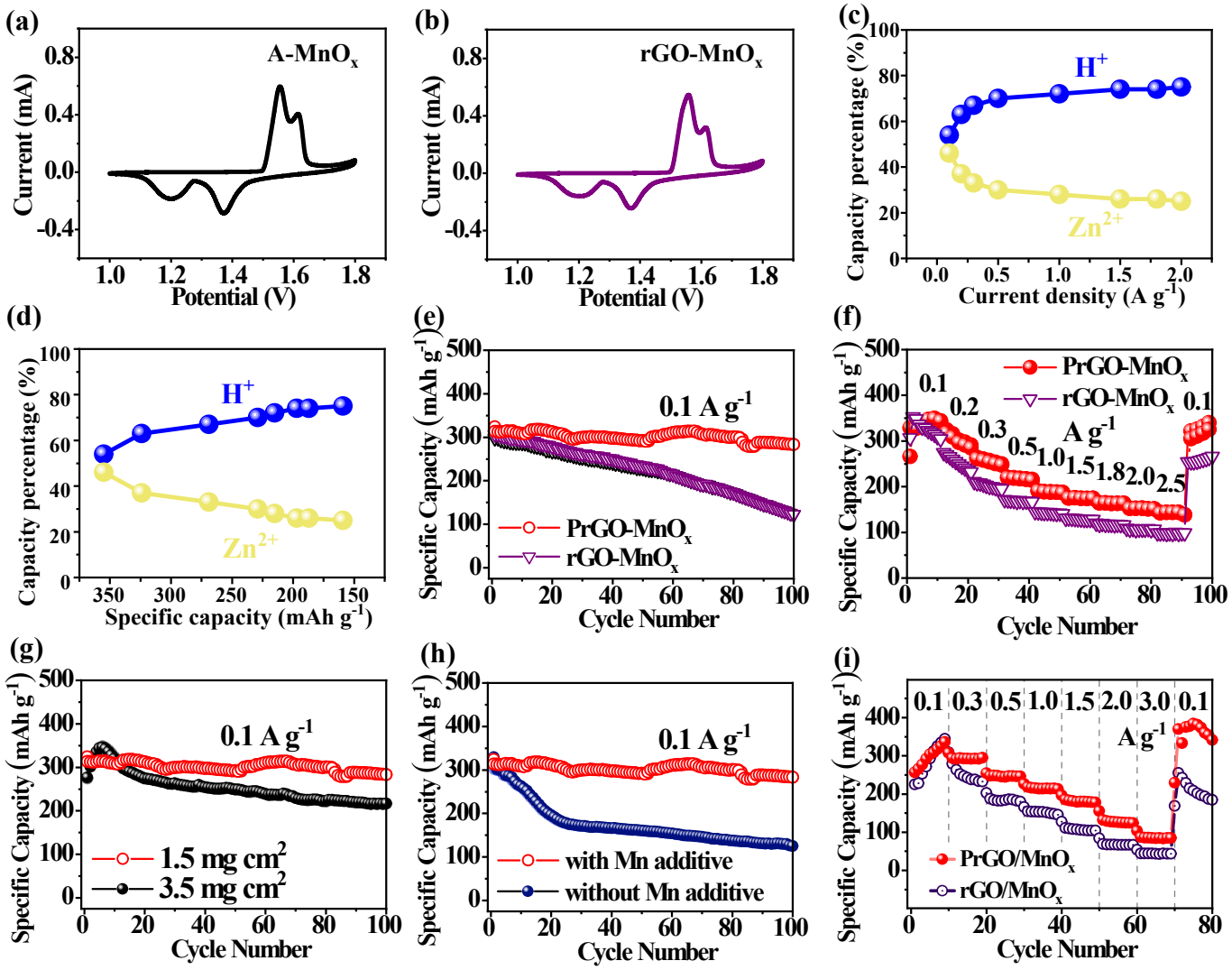

Fig. S8. CV curves of **(a)** A-MnO_x and (b) rGO-MnO_x. **(c, d)** Specific capacity contribution percentage of Zn^{2+} and H^+ at various current density from 0.1 to 2.0 A $g^{-1}$and at the corresponding specific capacity (all the data were read from the discharge/charge curves of PrGO-MnO_x electrode in figure 3c). Comparison of **(e)** rate performance and **(f)** cycling stability of the PrGO-MnO_x and rGO-MnO_x electrodes. **(g)** Electrochemical performance of PrGO-MnO_x with different mass loading (1.5 mg cm^{-2} vs. 3.5 mg cm^{-2}). **(h)** Cycling performance of PrGO-MnO_x electrode with Mn additive (2 M $C_2F_6O_6S_2Zn$ + 0.2 M $C_2F_6O_6S_2Mn$) and without Mn additive (2 M $C_2F_6O_6S_2Zn$). **(i)** Comparison of rate performance of the PrGO/MnO_x and rGO/MnO_x electrodes. The PrGO/MnO_x material was prepared via a mechanical ball-mill method as follows. Specifically, a 25 wt.% of PrGO and 75wt.% of A-MnO_x were added into a 50 mL stainless steel jar and ball-milled at the running speed of 450 rpm for 12 h with a ratio of balls weight to materials weight being 25: 1. The rGO/MnO_x was made under the same conditions but using the same amount of rGO to replace PrGO. As seen, the rate performance

of PrGO/MnOx is better than that of rGO/MnOx, especially at the high current density such as 2.0 and 3.0 A g^{-1}, indicating the enhanced ion diffusion efficiency and superior reaction kinetics of PrGO, and this performance also confirms that the material morphology of PrGO-MnOx is not the uppermost factor that affects the electrochemical performances.

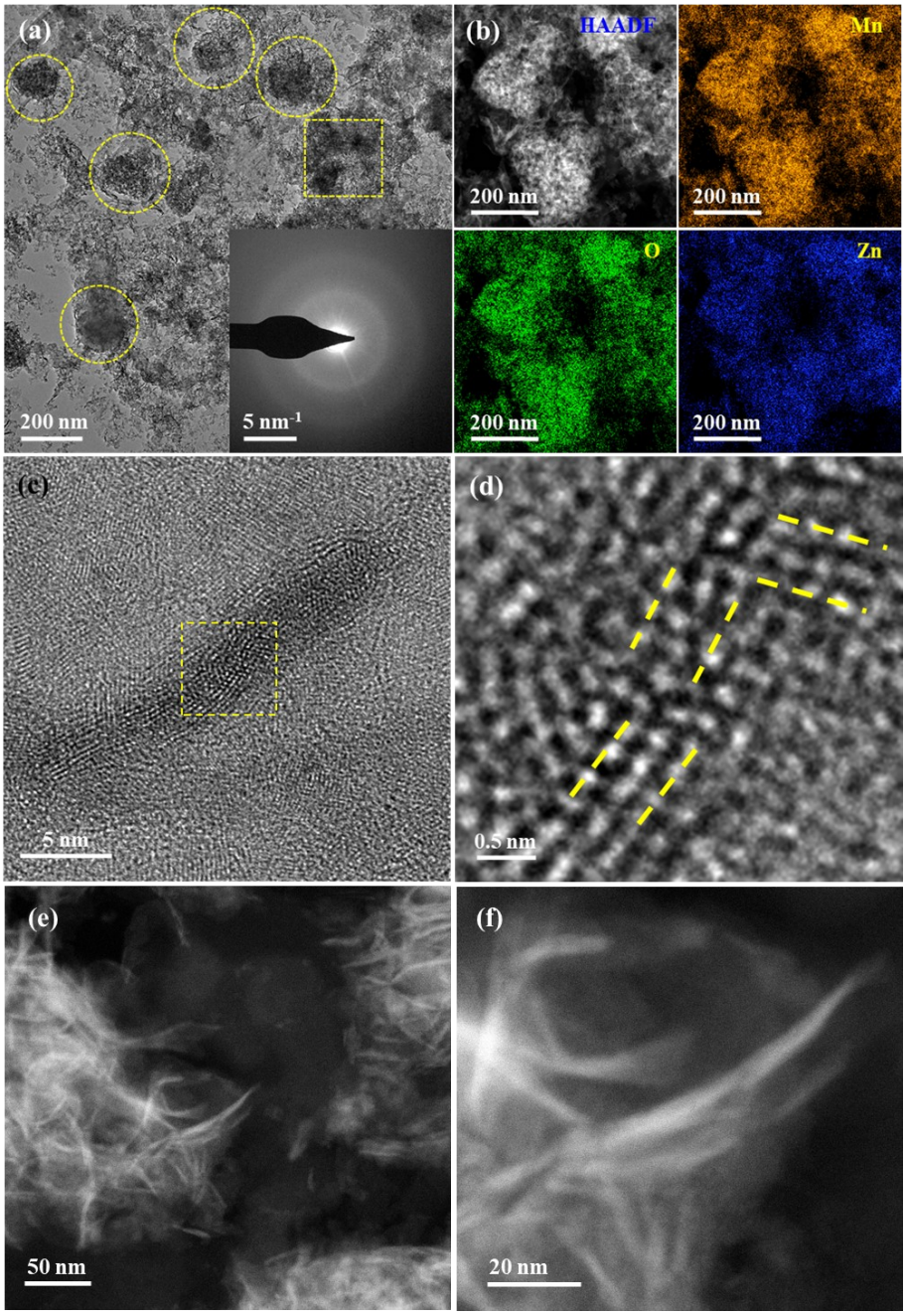

Fig. S9. (**a**,**b**) TEM and HRTEM images of PrGO-MnO_x electrode after 100 cycles at 0.2 A g^{-1} and corresponding SAED patterns (obtained from the squared area of the picture) as well as elemental mapping images of the PrGO-MnO_x electrode. (**c**,**d**) HRTEM image of the full-discharged PrGO-MnO_x electrode after 100 cycles at 0.1 A g^{-1}. (**e**,**f**) TEM images of the PrGO-MnO_x electrode after 2000 cycles.

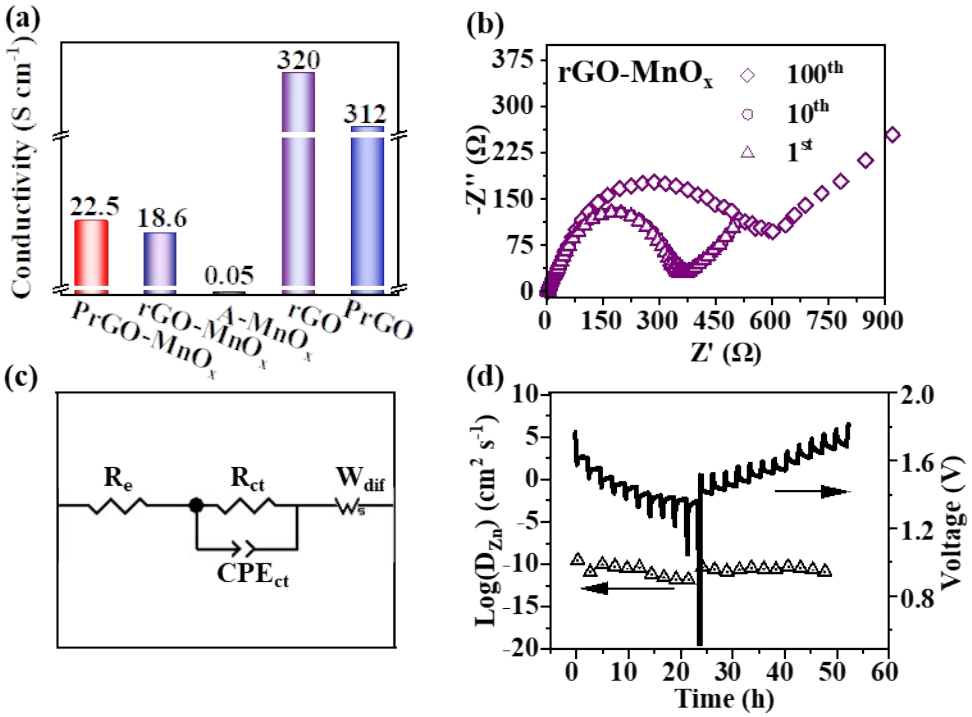

Fig. S10. (**a**) Comparison of electrical conductivity of PrGO-MnO_x, rGO-MnO_x, A-MnO_x, rGO and PrGO. (**b**) Nyquist plots of rGO-MnO_x electrode after various discharge/charge cycles from 1st to 100th. (**c**) The equivalent circuit diagram which is applied to fit all the Nyquist plots, where R_e/R_{ct}/W_{dif} represents the electrolyte-electrode resistance/charge transfer resistance/ions diffusion resistance, respectively. (**d**) GITT profiles and corresponding diffusion coefficient of A-MnO_x electrode at 50 mA g^{-1}.

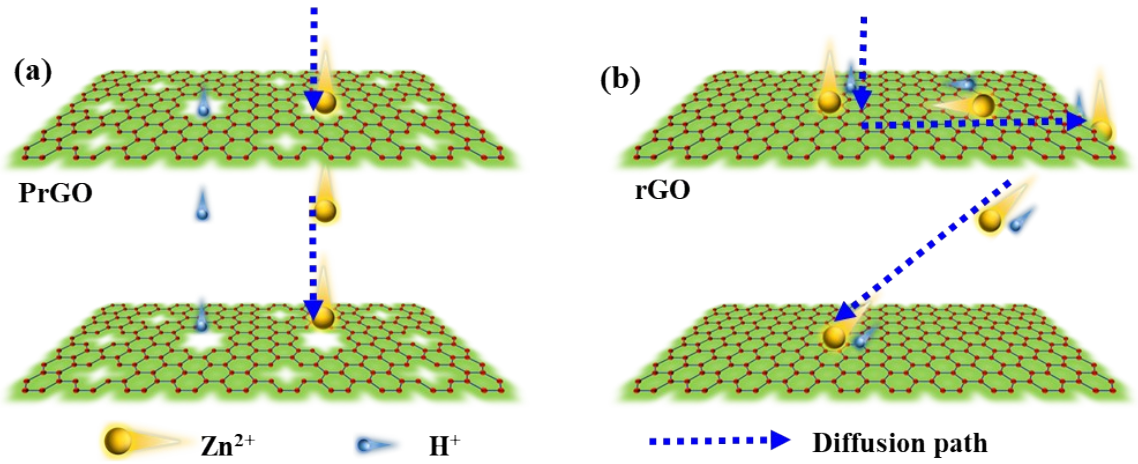

Fig. S11. Schematic illustration of H^+/Zn^{2+} diffusion path when they pass through (**a**) PrGO and (**b**) rGO. As shown, PrGO is more benefical for H^+/Zn^{2+} diffusion than rGO.

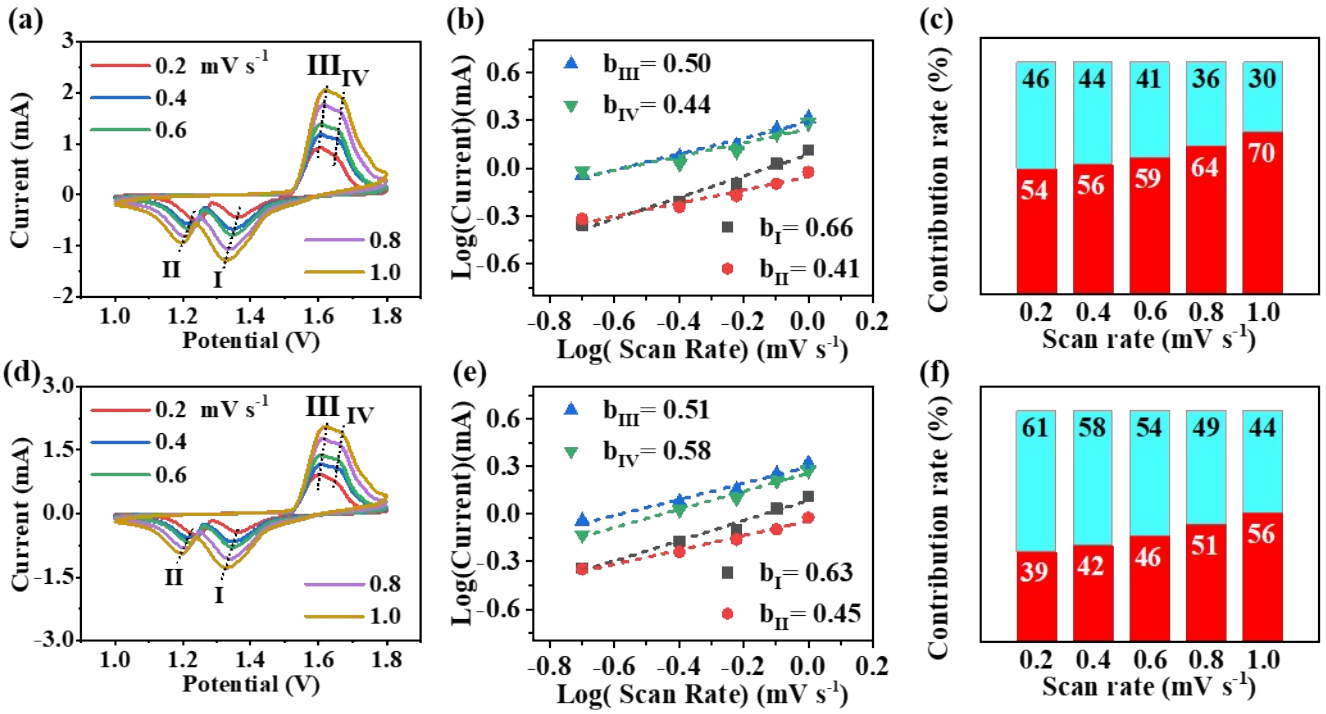

Fig. S12. (**a/d**) CV profiles of the rGO-MnO_x/A-MnO_x electrode at various scan rates from 0.2 to 1.0 mV s^{-1}. (**b/e**) Linear relationships between Log (redox peak current, mA) and Log (scan rate, mV s^{-1}) for rGO-MnO_x/A-MnO_x electrode. (**c/f**) Normalized capacity contribution ratio of rGO-MnO_x/A-MnO_x electrode at different scanning rates; The red and cyan bar represent the contribution of pseudocapacitance and diffusion, respectively.

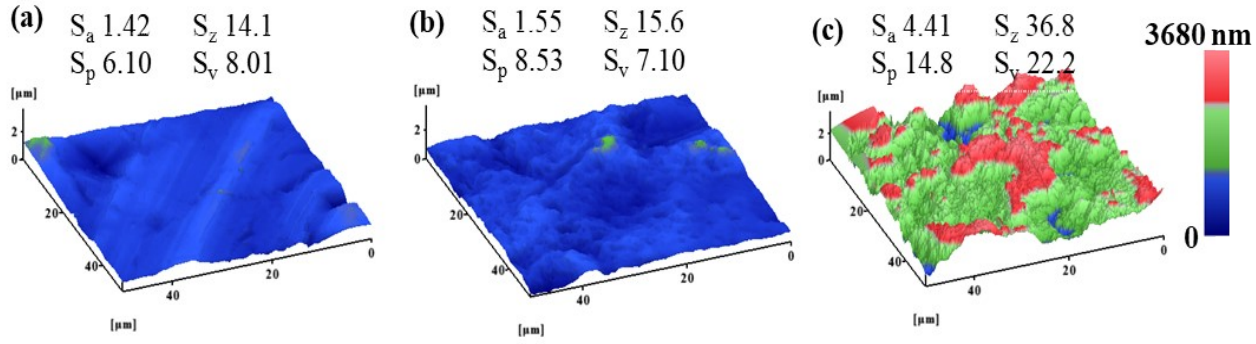

Fig. S13. Three-dimensional AFM images and corresponding surface roughness data of (**a**) pristine zinc foil, (**b**) zinc anode paired with PrGO-MnO_x cathode after 100 cycling under a current density of 100 mA g^{-1} and (**c**) zinc anode matched with A-MnO_x electrode cycled 100 times under the same current density.

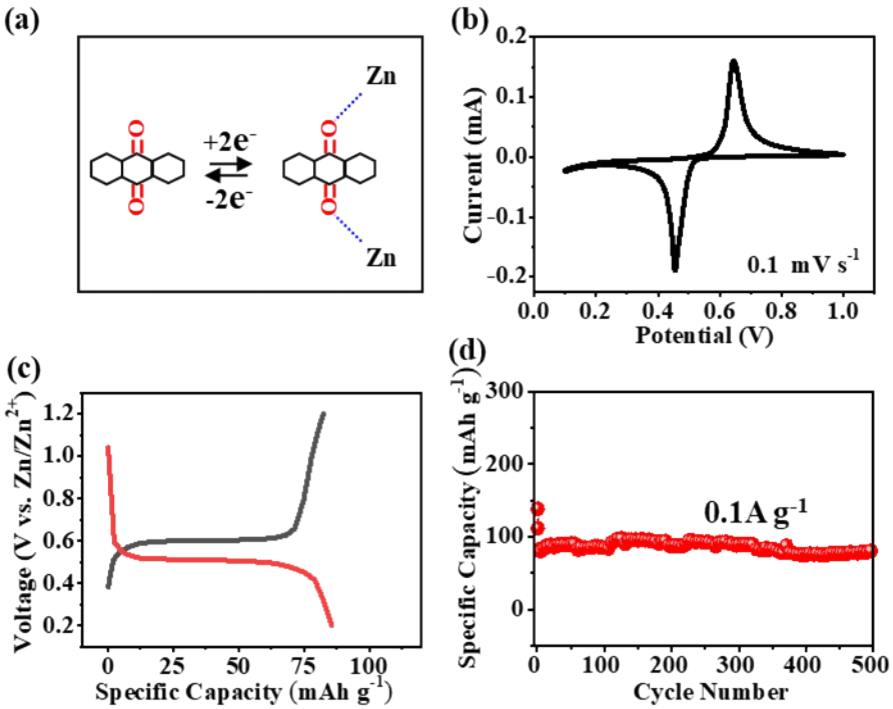

Fig. S14. (**a**) Structural formula of AQ and its mechanism of Zn-storage. (**b**) CV curves, (**c**) discharge-charge curves and (**d**) cycling performance of AQ//Zn cell.

References

S1. C. An, Y. Yuan, B. Zhang, L. Tang, B. Xiao, Z. He, J. Zheng, J. Lu, *Adv. Energy Mater.*, 2019, 9, 1900356.

S2. Z. Bo, X. Shuai, S. Mao, H. Yang, J. Qian, J. Chen, J. Yan, K. Cen, *Sci. Rep.*, 2014, 4, 4684.

S3. M. Wang, Z. Wang, R. Jia, Y. Yang, F. Zhu, Z. Yang, Y. Huang, X. Li, W. Xu, *Appl. Surf. Sci.*, 2018, 456, 379.

S4. X. Wang, L. Jiao, K. Sheng, C. Li, L. Dai, G. Shi, *Sci. Rep.*, 2013, 3, 1996.

S5. Z.Q. Wang, M.S. Wang, Z.L. Yang, Y.S. Bai, Y. Ma, G.L. Wang, Y. Huang, X. Li, *ChemElectroChem*, 2017, 4, 345.